

Chapter 2

Experimental Aspects

2.1 The Daresbury MEIS Facility

All MEIS experiments in this work were performed at the Daresbury MEIS facility, located at the CCLRC Daresbury Laboratory, Warrington, UK [1, 2]. The facility is a relatively new laboratory originally developed as a collaboration between the Universities of Warwick and Salford to provide a resource to the UK surface science community. The facility was commissioned on 1st April 1996. A description of the technique of MEIS itself may be found in Chapter 3; this section describes the MEIS facility.

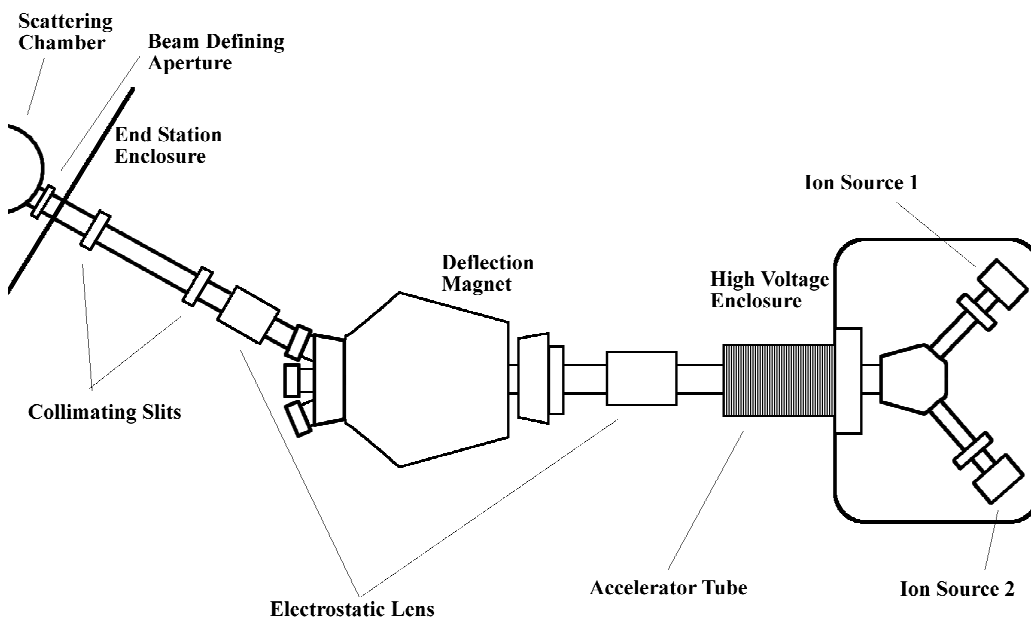


Figure 2.1: Schematic diagram of the Daresbury MEIS facility beam line. Ions are produced by a duoplasmatron source and accelerated to around 100 keV. The ion beam is then focused and collimated before entering the scattering chamber.

The Daresbury MEIS facility comprises an ion source, beam line and end user experimental station. The ion source is a hot-cathode duoplasmatron source and accelerator capable of operating at up to 400 keV, which were derived from the decommissioned Nuclear Structure Facility previously located at Daresbury. The ion source and accelerator are connected via the beam line to a user end station consisting of several interconnected UHV chambers. A schematic diagram of the ion source and beam line is shown in Figure 2.1. The collimating slits and beam defining aperture ensure a beam divergence of $< 0.1^\circ$ and size of $0.5 \times 1.0 \text{ mm}^2$ (vertical \times horizontal) at the sample. The ion source, beam line components and detector are all remotely computer controlled from within the end station.

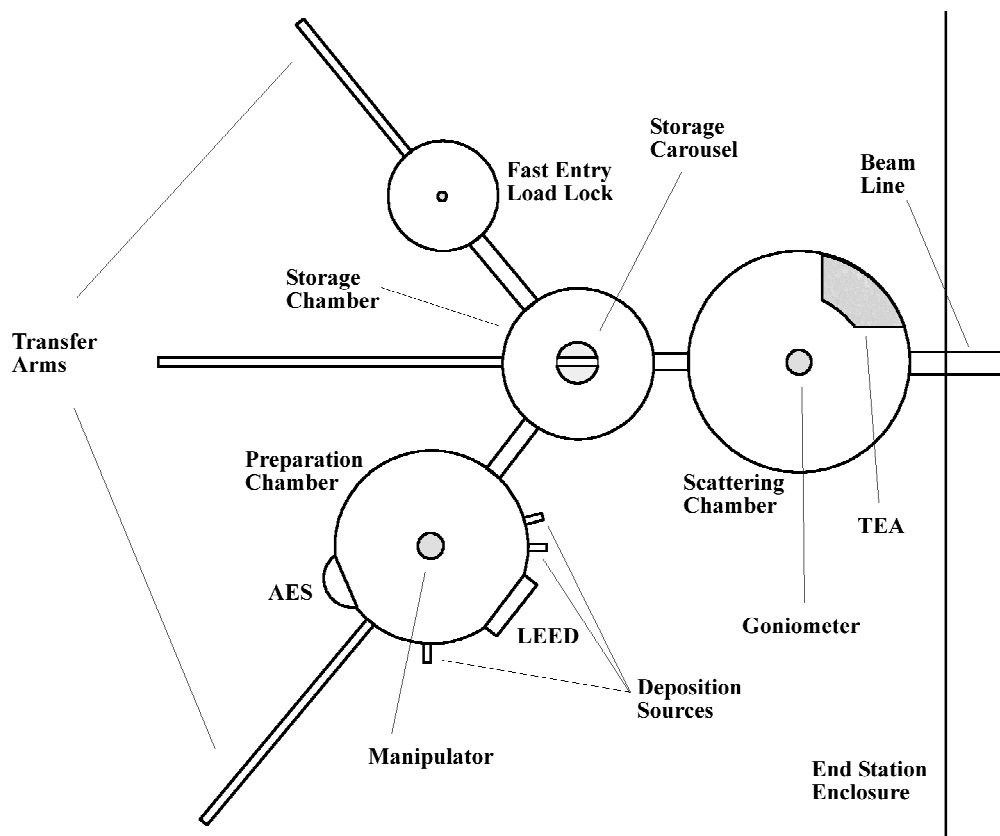


Figure 2.2: Schematic diagram of the Daresbury MEIS facility user end station. The ion beam enters at the main scattering chamber. Sample preparation is performed in a separate chamber and sample storage and fast entry is also available.

The end station itself consists of three UHV chambers and a fast entry load lock, connected by transfer arms to allow for free movement of samples. The chambers are isolated from one another by means of viton gate valves when sample transfer is not taking place. A schematic of the end station is shown in Figure 2.2. The load lock allows for a sample to be put into the UHV system within about 30 minutes. It also contains simple heating facilities to degas sample holders and samples in preparation for UHV compatibility. The sample storage chamber contains a rotating carousel capable of holding up to six samples. One of the storage positions on this carousel offers electron-beam sample heating. The base pressure of this chamber is around 3×10^{-10} mbar after bakeout, being pumped by a combination of a rotary backed turbomolecular pump and a TSP.

The sample preparation chamber operates at a base pressure of 1×10^{-10} mbar, being pumped in a similar manner to the storage chamber. The chamber is equipped with a sample manipulator offering lateral translation and sample rotation. The system offers a rear view LEED, AES, e^- -beam heating of samples, and the facility to Ar^+ ion bombard samples. A variety of deposition sources can also easily be attached to the chamber for sample preparation. Sample temperature may be monitored by means of an external infrared pyrometer.

The scattering chamber operates at a base pressure of 1×10^{-10} mbar. Like the other UHV chambers this is pumped by a combination of turbomolecular pump and TSP. The chamber is equipped with a goniometer (high precision manipulator) allowing three degrees of sample rotation to within 0.1° , as well as XYZ-translation. Immediately the ion beam enters this chamber there is a beam monitor consisting of vertical strands, 50 μm diameter, of gold coated tungsten (shielded at -300 V to suppress secondary electron loss). This measures a fixed amount of the ion beam to give a measure of the current transmitted to the sample.

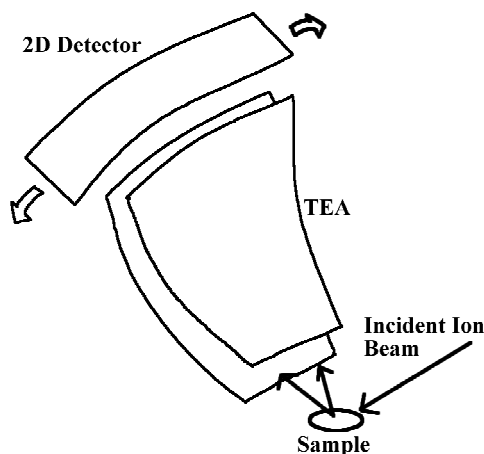


Figure 2.3: The toroidal electrostatic analyser and 2D detector produce the 2D data sets in MEIS experiments. Ions entering the detector are bent through 90° before hitting a set of channel plates which amplify the charge so it may be detected by the 2D detector plate.

The scattering chamber also contains the TEA. This admits the scattered ions over a 27° window and an energy window of 2 % of the pass energy. The operation of the TEA is similar to a hemispherical analyser. The ions are electrostatically bent through 90° where they impinge upon a set of channel plates to produce an amplified charge which is detected by a position sensitive detector plate, hence producing the 2D map of scattered ions (Figure 2.3).

2.2 Scanning Tunnelling Microscopy

2.2.1 General Principle

STM was developed in the early 1980s, initially by G. Binnig and H. Rohrer [3, 4]. It has rapidly become one of the main—and most powerful—tools available to the surface scientist [5-10].

The scanning tunnelling microscope operates based on the phenomenon of quantum mechanical tunnelling of electrons [11-14]. From a quantum mechanical point of view the electrons may be described as wave functions and have a finite probability of tunnelling through a potential barrier in a classically

forbidden way. STM utilises this by bringing a metallic tip close (to within about 1 nm) to the surface of interest. If a bias voltage is then applied between tip and sample electrons are free to tunnel through the vacuum gap from the tip to the surface under investigation (or vice versa). This results in a tunnelling current (of the order of a few nanoamps)

$$I_T \propto V_T \exp(-A\Phi^{1/2}s) \quad (2.1)$$

where Φ is the tunnelling barrier height and s the tunnelling barrier width.

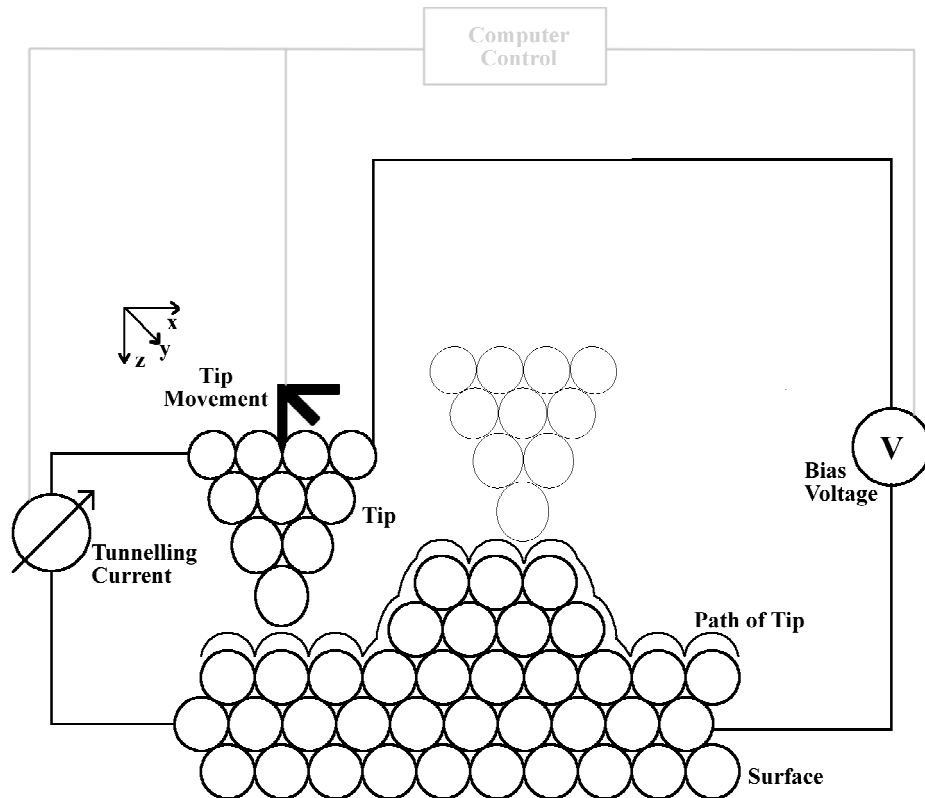


Figure 2.4: The general operation of the scanning tunnelling microscope in constant current mode. As the tip is scanned across the surface its z-position is adjusted to maintain a constant tunnelling current. This results in the tip following the contours of the surface.

The term A is given by

$$A = \left(\frac{4\pi}{h} \right) \sqrt{2m} = 1.025 \text{ \AA}^{-1} \text{ eV}^{-1/2} \quad (2.2)$$

m being the free electron mass and h Planck's constant.

The barrier width is determined by the tip-sample separation and the barrier height by the work function. For a typical work function of a few electron volts a change in the barrier width (i.e. tip-sample separation) of about an Ångstrom produces an order of magnitude change in tunnelling current.

If the tunnelling current is monitored as the tip is scanned across the surface in a raster pattern this sensitivity of the tunnelling current to the tip-sample separation makes it possible to map out the surface topography. This mode of operation, in which the surface is mapped using the tunnelling current, is known as constant height mode. In fact it is more normal to maintain a constant tunnelling current by adjusting the tip "height", or z -position, in a feed back loop and use this position as a measure of the topography in producing a greyscale image as the tip is scanned across the surface. This mode of operation is known as constant current mode. Figure 2.4 schematically shows the principle of operation in this mode. While this mode of operation is not as fast as constant height mode it has the advantage that the tip follows the corrugation of the surface and so reduces the likelihood of tip crashes as the tip is able to move over large islands and step edges.

2.2.2 Theory

The theory of STM has been given by Tersoff and Hamann [13, 14]. Perturbation theory gives a first order for the tunnelling current given by

$$I = \frac{2\pi e}{\hbar} \sum_{\mu\nu} f(E_{\mu}) [1 - f(E_{\nu} + eV)] |M_{\mu\nu}|^2 \delta(E_{\mu} - E_{\nu}) \quad (2.3)$$

where $f(E)$ is the Fermi function, V the bias voltage, $M_{\mu\nu}$ is the tunnelling current matrix element between the states ψ_{μ} of the probe and ψ_{ν} of the surface and E_{μ} and E_{ν} are the energies of the states ψ_{μ} and ψ_{ν} respectively (in the absence of tunnelling).

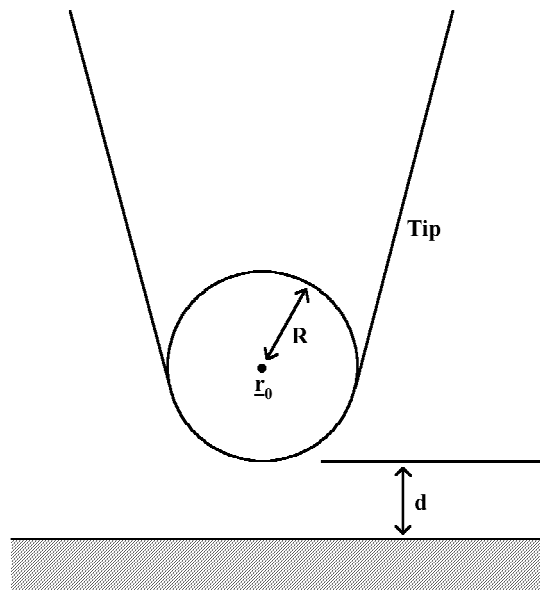


Figure 2.5: The model tip used in the calculations of Tersoff and Hamann [13, 14]. The tip is taken as a spherical potential well of radius R , centred at \mathbf{r}_0 a distance d above the surface.

In the limits of low temperature and voltage Equation 2.3 becomes

$$I = \frac{2\pi}{\hbar} e^2 V \sum_{\mu\nu} |M_{\mu\nu}|^2 \delta(E_\nu - E_F) \delta(E_\mu - E_F) \quad (2.4)$$

E_F being the Fermi energy.

The probe tip was modelled as shown in Figure 2.5. The tip is taken to be a spherical potential well centred about \mathbf{r}_0 a distance d from the surface, with a radius of curvature R . By expanding the tunnelling matrix element as described by Bardeen [15] and writing the wave functions ψ in appropriate forms, Tersoff and Hamann were able to show that Equation 2.4 becomes

$$I = 32\pi^3 \hbar^{-1} e^2 V \phi^2 D_t(E_F) R^2 k^{-4} e^{2kR} \sum |\psi_\nu(\mathbf{r}_0)|^2 \delta(E_\nu - E_F) \quad (2.5)$$

Here D_t is the density of states per unit volume of the tip, ϕ is the work function (it is assumed the work functions of tip and sample are the same), and the term k is given by

$$k = \frac{(2m\phi)^{1/2}}{\hbar} \quad (2.6)$$

Equation 2.5 has important consequences. As $|\psi_\nu(\mathbf{r}_0)|^2 \propto e^{-2k(R+d)}$ the conductance σ is seen to be

$$\sigma \propto e^{-2kd} \quad (2.7)$$

which reproduces the exponential dependence on tip-sample separation seen in Equation 2.1.

Although the theory developed by Tersoff and Hamann is useful it is too simplistic to describe some aspects of STM. For instance, the predicted lateral resolution of the STM is around 5–6 Å, which is clearly larger than can be

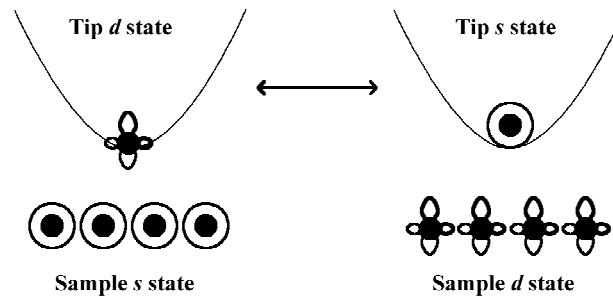


Figure 2.6: Qualitative description of the reciprocity principle. Probing surface s states with a tip d state is equivalent to probing d states with a tip s state.

achieved in practice. In order to explain this discrepancy, Chen developed a theory of the STM in which the electronic states of the probe tip were realistically considered [11, 12]. Chen showed that the resolution of the STM is due to d or p states of the probe tip. These states cause the increased resolution because of the “reciprocity principle” in STM: If the tip and sample states are interchanged then the image should be identical. The explanation is shown qualitatively in Figure 2.6. If there is a d state on the tip it traces not the charge density of the surface but that of a non-existent surface with a d state on each atom. It is this which allows higher resolutions than those predicted by theory just considering the s states. It is this effect which makes a metal such as W, a d band metal, an ideal material for STM probes.

It is interesting that the very reason the STM can achieve such very high lateral resolution is also one of the most important difficulties in STM. When considering the topography of a surface obtained by STM one must bear in mind that not only the surface but also the tip electronic structure plays a role. The image obtained is in reality a convolution of the sample and tip electronic states. It is the change in the tip electronic structure when contaminants are picked up or lost that can cause an abrupt change in resolution during scanning. And on occasion it is possible that the images obtained have little relation with the surface under investigation and much more to do with the tip being used.

2.2.3 Scanning Tunnelling Spectroscopy

As electronic effects are so important in the tunnelling process, and the tunnelling current exhibits a bias voltage dependence, images taken at different biases may show striking differences. This is especially evident when considering STM images obtained when the sample is positively biased (in which case empty states of the sample are being imaged) compared to negatively biased (in which case filled states are imaged). It is this dependence that results, for instance, in the difference between STM images of the familiar Si(111) 7×7 reconstructed surface. In images obtained with negative sample bias one half of the reconstructed unit cell appears darker than the other; while for positive sample bias the two halves have approximately equal brightness (see for example Avouris *et al* [16], Tromp *et al.* [17], Figure 2.7).

Whilst some information may be gained by examining a surface under different bias conditions (most usually by scanning with one bias in the “forward” direction and then a different bias as the tip makes the return journey in the

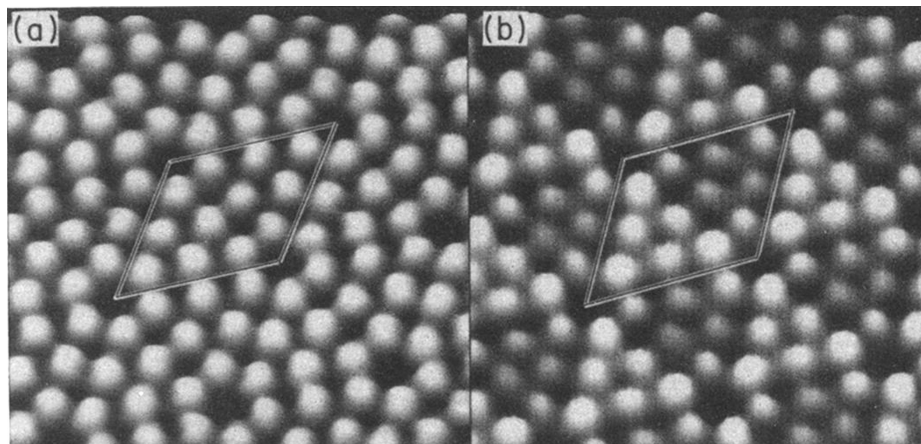


Figure 2.7: Bias condition dependence of STM imaging, in the case of the Si(111) 7×7 surface. (a) Unoccupied states with the sample biased at +1.5 V. (b) Occupied states with the sample biased at -1.5 V. The unit cell is marked in each case. Note that in the case of (b) a difference is clear between the faulted and unfaulted half of the unit cell, whilst in (a) the two halves appear the same. From Avouris & Wolkow [16].

“backward” direction) it is possible to extend the technique in a more quantitative manner. The technique of scanning tunnelling spectroscopy is one such way [7, 11, 18, 19]. In STS the tip is momentarily held stationary during the scan and the feedback loop adjusting the tip height is turned off. The tunnelling current is then measured as the bias voltage is ramped to give a plot of current versus voltage. By performing this procedure at every point on a normal STM scan (or at a grid of points) it is possible to gain spatially resolved spectroscopic information about the surface of interest. Of course due to the nature of the interaction it is important to be aware that the tip electronic structure may also influence STS data, just as it might an ordinary STM image.

2.2.4 *Apparatus*

The experiments reported in this work were performed using two STMs within the Surface Science Group at the University of York. Both are commercial instruments supplied by Omicron GmbH. The first is an Omicron STM 1. This STM is housed in an UHV side chamber attached to an UHV sample preparation chamber (Figure 2.8). The system is pumped by a rotary backed diffusion pump and a TSP with the base pressure after bakeout being around 1×10^{-10} mbar. The preparation chamber offers the standard surface science equipment such as a rearview LEED capable of also performing AES, sample e^- -beam and direct current heating facilities, Ar^+ bombardment and the option to attach a variety of deposition sources. Samples may be transferred in vacu between the preparation chamber and the STM. There is also a storage carousel where up to eight samples may be held.

The STM tip is scanned across the sample surface by means a tripod arrangement of three piezoelectric tubes, one each controlling the x-, y- and z-motion. The sample itself is mounted on further piezoelectric legs running in tracks. By applying a skewed voltage pulse to these legs it is possible to move the sample in a slip-stick motion to facilitate controlled macroscopic approach to the tip. The scanning, bias voltage, etc are controlled by an interface to a HP-UX computer.

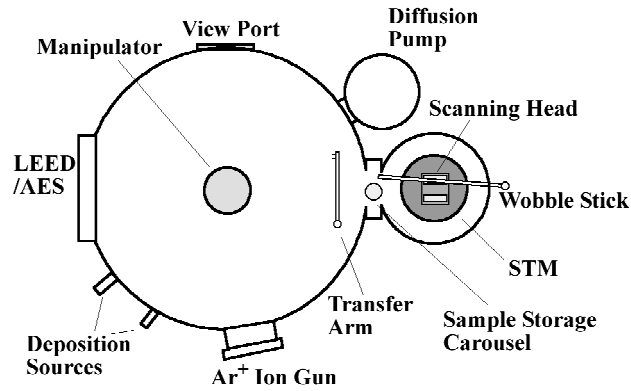


Figure 2.8: Schematic diagram of the STM 1 system. The STM is housed in a UHV side chamber attached to a UHV sample preparation chamber equipped with LEED, AES and deposition sources.

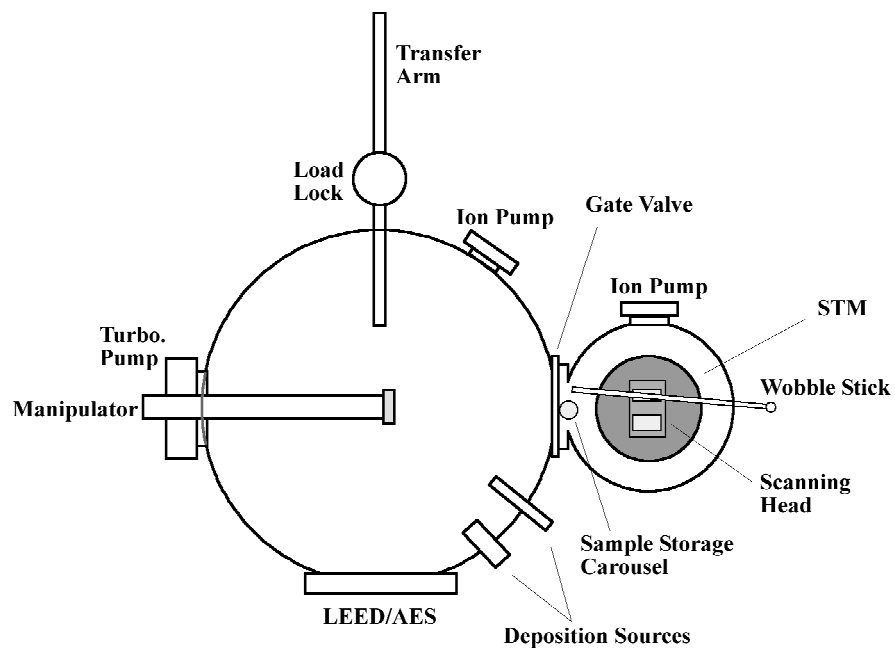


Figure 2.9: Schematic diagram of AFM/STM systems used. The UHV STM side chamber may be isolated from the main UHV sample preparation chamber. Samples may be quickly exchanged in and out of the system using a load lock

The entire UHV system is vibrationally isolated by mounting on three tyre inner tubes and housed within a purpose built hut in the laboratory, to ensure mechanical stability whilst the STM is in operation. The STM stage itself magnetically damped *in vacu* to further reduce vibrations.

The second instrument is a newer Omicron AFM/STM. It is also housed in an UHV side chamber attached to an UHV preparation chamber (Figure 2.9). The preparation chamber again offers LEED, AES, ion bombardment and sample heating. Samples may be transferred from the preparation chamber to the STM by means of a manipulator and wobble stick. The STM chamber may be isolated from the preparation chamber by means of a gate valve during sample preparation, as it is independently pumped by an ion pump. The main chamber is pumped by a combination of a second ion pump and a rotary backed turbomolecular pump. The base pressure achieved after bakeout is in the region of 1×10^{-10} mbar. The system also has a vacuum load lock to allow expedient sample entry and removal and a sample storage carousel within the STM chamber.

The AFM/STM is of a similar design to the STM 1 but with additional parts to facilitate AFM. The main difference between the two instruments is that where the STM 1 scanning is driven by three piezoelectric tubes, in the AFM/STM a single piezoelectric tube produces the motion in all three axis. Also it is the sample, rather than the tip itself, which is moved in the scanning process. The system is controlled by an interface to a PC. The system is again vibrationally isolated. Both the STM 1 instrument and the AFM/STM have routinely achieved atomic resolution of clean semiconductor surfaces.

2.3 Low Energy Electron Diffraction

One of the most widely used techniques in surface physics is that of LEED [20-22]. LEED, as the name suggests, involves the diffraction of electrons from the surface. A beam of electrons with energy in the region of ~20–300 eV is made to fall onto the sample normal to the surface. At this energy range the de Broglie

wavelength of the electrons is comparable with atomic spacings.

The basic principle underlying LEED may then be seen by considering the simple one dimensional case, Figure 2.10. With the electron beam normal to the one dimensional array there will occur constructive interference of backscattered electrons when the Bragg condition is met,

$$a \sin(\theta) = n\lambda \quad (2.8)$$

where θ is the backscattering angle, a the interatomic spacing, n an integer and λ is the electron wavelength given by

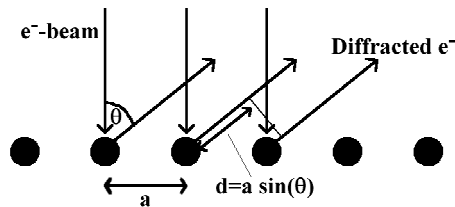


Figure 2.10: Simple diffraction in 1D. Constructive interference occurs when the Bragg condition is met, i.e. path difference $d = n\lambda$, λ being the electron wavelength and $n = \dots -2, -1, 0, 1, 2, 3, \dots$

$$\lambda = \frac{h}{(2m.e.V)^{1/2}} \quad (2.9)$$

Extending to two dimensions constructive interference will occur when both $n_a\lambda = a \sin(\theta_a)$ and $n_b\lambda = b \sin(\theta_b)$, a and b being the primitive interatomic spacings. This may be most clearly seen by considering the familiar Ewald sphere (Figure 2.11). In the 2D case each 2D lattice point is associated with a rod normal to the surface. The Bragg condition is met when $\mathbf{k}_i - \mathbf{k}_s$ is equal to a vector of the 2D reciprocal lattice, \mathbf{g} , where \mathbf{k}_i and \mathbf{k}_s are the wave vectors of the incident and scattered electron, respectively. As can be seen from Figure 2.11 this occurs when the sphere crosses a reciprocal lattice rod.

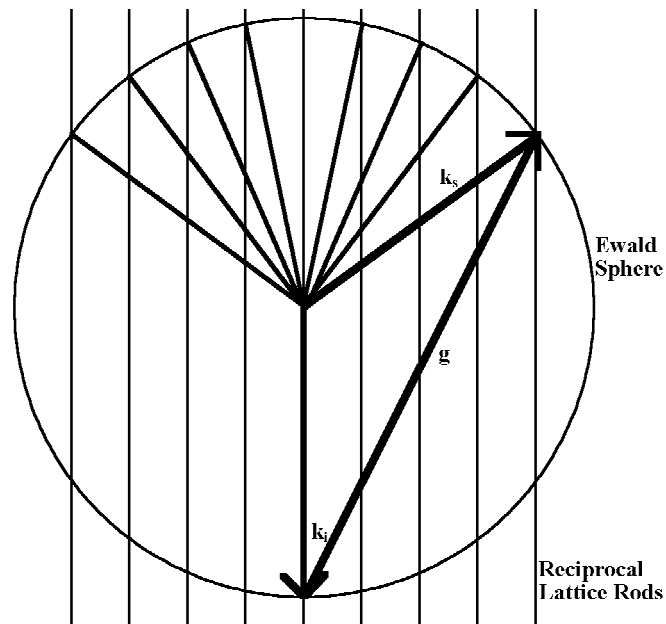


Figure 2.11: The Ewald sphere for elastic scattering in 2D. The bragg condition $k_i - k_s = g$ is met whenever the sphere crosses a reciprocal lattice rod.

This results in set of rods in a two dimensional array. By observing across these rods a set of points is seen (see Figure 2.12 for an example). In two dimensions the LEED pattern is therefore an image of the surface reciprocal net.

The LEED pattern obtained reflects the surface atomic arrangement; the pattern of spots is dependent on the surface reconstruction present (if any) and the spacing between spots as a function of electron energy inversely relates to the real space atomic spacings. Determining atomic structure from LEED is far from straight forward. The electrons scatter from not only the first purely two dimensional layer but also deeper layers and also undergo multiple elastic scattering. The simple kinematic theory outlined above is therefore not sufficient to describe the scattering.

Original in colour

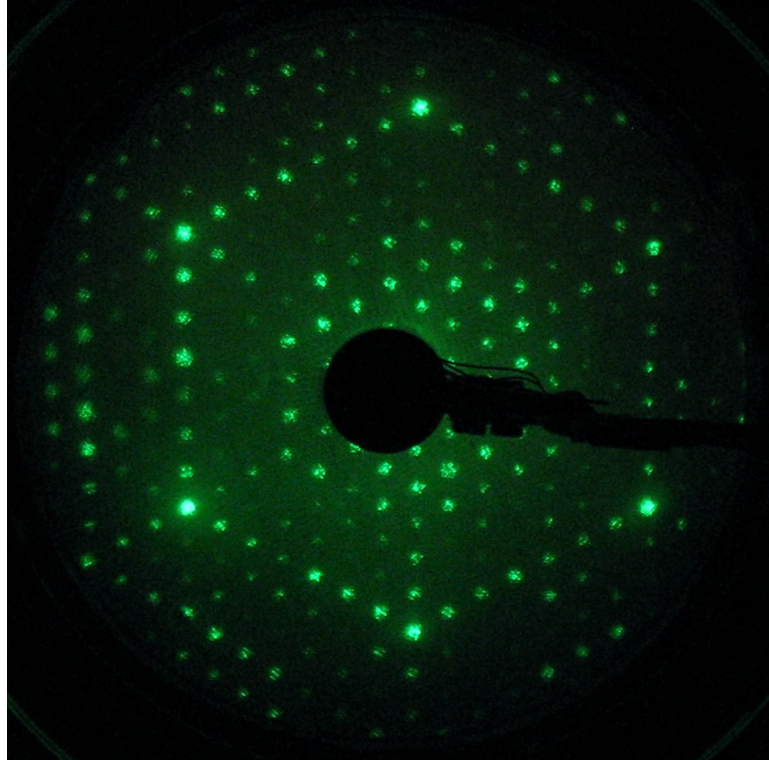


Figure 2.12: An example LEED pattern [24], showing the diffraction pattern from the clean Si (111) 7×7 surface with incident electron energy of 40 eV. Note that the periodicity of the surface is immediately apparent.

It is possible to use LEED in a more quantitative manner by observing the intensity of a spot as a function of the incident electron energy to give an $I(V)$ curve [23]. Such a practice can allow the surface structure to be fully determined using LEED but the process is complicated and requires computer simulation of trial structures. It is much more usual to use LEED as a diagnostic tool to indicate the reconstruction and quality of a surface prior to the use of some other technique.

A typical LEED apparatus is shown schematically in Figure 2.13. The grids G1, G2 and G3 and the screen are concentric hemispheres centred around the sample. Diffracted beams are accelerated between the grid G1 and the screen in order to have enough energy to cause a fluorescence at the screen. The grids G2 and G3

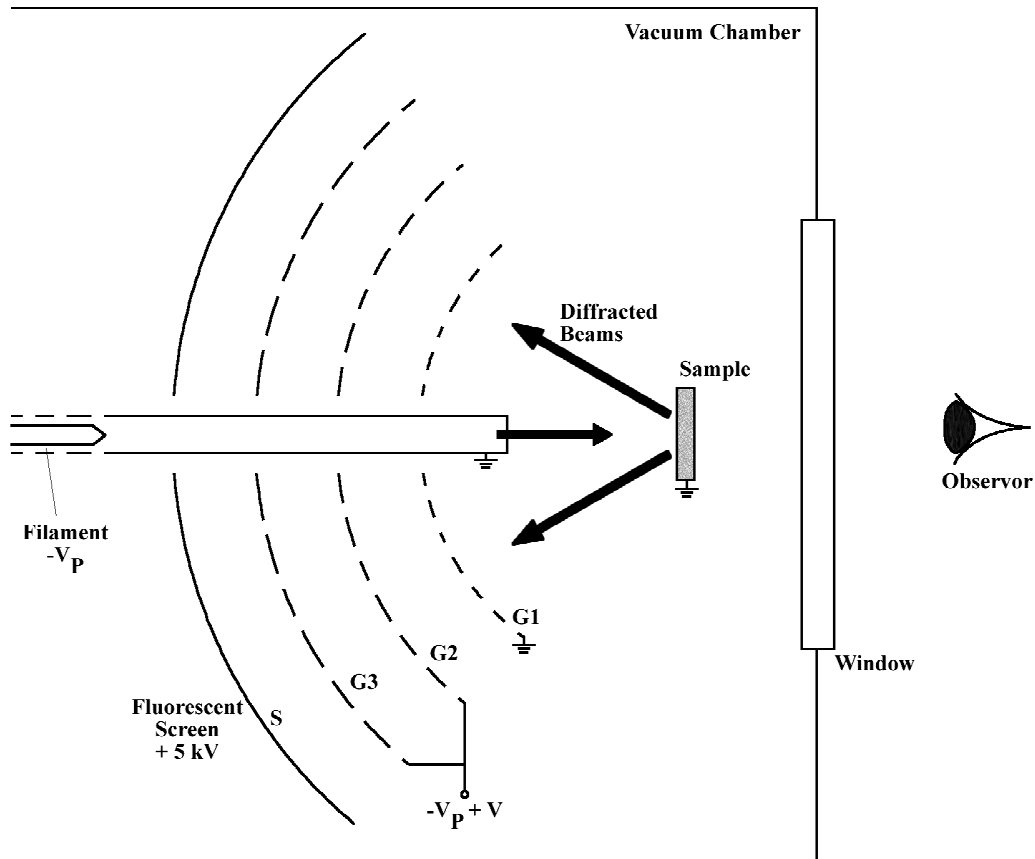


Figure 2.13: Typical LEED apparatus. Electrons are diffracted from the sample and accelerated between the grid G1 and the fluorescent screen. The grids G2 and G3 filter out the lower energy, inelastically scattered electrons to reduce the background. It is often the case that the fluorescent screen is deposited on a window so that the pattern may be viewed through the glass to avoid the problems with the screen being obscured by the sample mountings.

act to filter out the lower energy inelastically scattered electrons which would contribute nothing but a diffuse background to the LEED pattern. Often the fluorescent screen is deposited on a glass section allowing the diffraction pattern to be observed through the glass and screen in order to avoid the problems of the sample mounting arrangement obscuring the screen. This arrangement is known as a “reverse view” LEED.

References

1. P. Bailey, T. C. Q. Noakes and D. P. Woodruff, *Surf. Sci.* **426** 358 (1999)
2. D. Brown, T. C. Q. Noakes, D. P. Woodruff, P. Bailey and Y. Le Goaziou, *J. Phys. Condens. Matter* **11** 1889 (1999)
3. G. Binnig, H. Rohrer, Ch. Gerber and E. Weibel, *Phys. Rev. Lett.* **49** 57 (1982)
4. G. Binnig and H. Rohrer, *Surf. Sci.* **126** 236 (1983)
5. S. F. Alvarado, *Surf. Rev. Lett.* **2** 607 (1995)
6. P. A. Bennett and H. von Känel, *J. Phys. D: Appl. Phys.* **32** R71 (1999)
7. Ph. Avouris and I. -W. Lyo, *Studying surface chemistry atom-by-atom using the scanning tunneling microscope*, in *Chemistry and Physics of Solid Surfaces*, p. 371, Springer-Verlag: Berlin (1990)
8. R. J. Hamers, *STM on Semiconductors*, in *Scanning Tunneling Microscopy I*, H. J. Guntherodt & R. Wiesendanger, (Eds.) Springer-Verlag: Berlin (1992)
9. R. Wiesendanger, *Scanning probe microscopy and spectroscopy : methods and applications*, Cambridge University Press 637 (1994)
10. W. D. Schneider, *Surf. Sci.* **514** 74 (2002)
11. C. J. Chen, *J. Vac. Sci. Technol. A* **6** 319 (1988)
12. C. J. Chen, *Phys. Rev. Lett.* **65** 448 (1990)

13. J. Tersoff and D. R. Hamann, *Phys. Rev. B* **31** 805 (1985)
14. J. Tersoff and D. R. Hamann, *Phys. Rev. Lett.* **50** 1998 (1983)
15. J. Bardeen, *Phys. Rev. Lett.* **6** 57 (1961)
16. Ph. Avouris and R. Wolkow, *Phys. Rev. B* **39** 5091 (1989)
17. R. M. Tromp, R. J. Hamers and J. E. Demuth, *Phys. Rev. B* **34** 1388 (1986)
18. N. D. Lang, *Phys. Rev. B* **34** 5947 (1986)
19. S. P. Tear, *Scanning Probe Spectroscopies*, in *Spectroscopy for Surface Science*, p. 121, R. J. H. Clark & R. E. Hester, (Eds.) John Wiley & Sons (1998)
20. M. Prutton, *Introduction to Surface Physics*, Oxford University Press (1994)
21. D. P. Woodruff and T. A. Delchar, *Modern Techniques of Surface Science*, Cambridge University Press (1986)
22. A. Zangwill, *Physics at Surfaces*, Cambridge University Press (1988)
23. J. B. Pendry, *Low Energy Electron Diffraction: The Theory and Its Application to Determination of Surface Structure*, Academic Press (1974)
24. Courtesy of E. W. Perkins, *Unpublished* (2005)